Figure S1

A

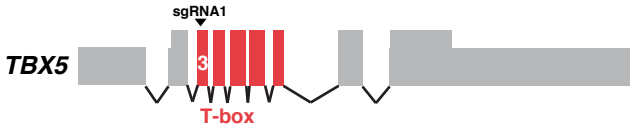

B

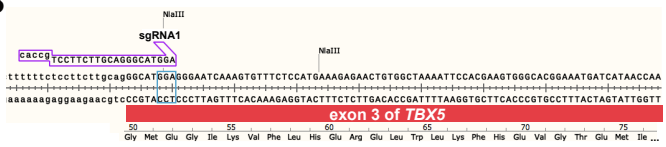

C

2bp insertion allele for *TBX5*$^{in/+}$

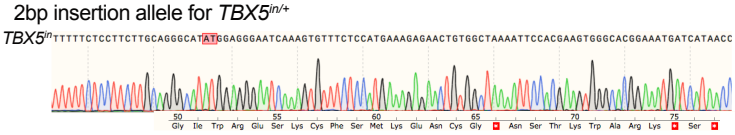

D

1bp insertion for *TBX5*$^{in/del}$

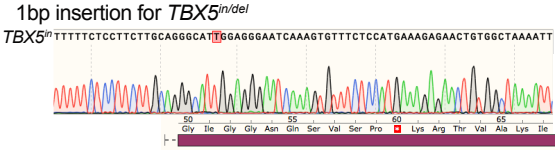

E

8bp deletion for *TBX5*$^{in/del}$

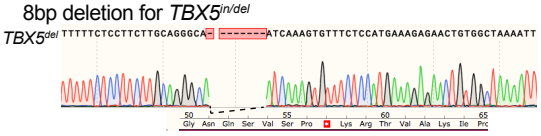

F

		Genotype	Translation
	WTC11	+/+	
+ Cas9	Control	+/+	
	TBX5$^{in/+}$	ins 2bp/+	p.M51fs*16/+
	TBX5$^{in/del}$	ins 1bp / del 8bp	p.M51fs*10/p.M51fs*7
	TBX5$^{PuR/PuR}$	ins *PGK-PuroR*/ins *PGK-PuroR*	

G

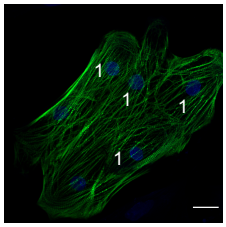

Score 1:
intact myofibrils,
mostly aligned in parallel

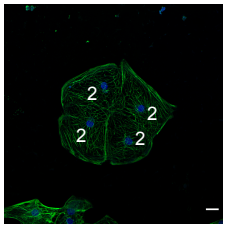

Score 2:
intact myofibrils,
many not in parallel

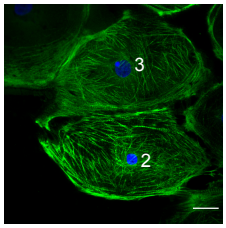

Score 3:
myofibrillar fragmentation or
aggregation < 50% cell volume

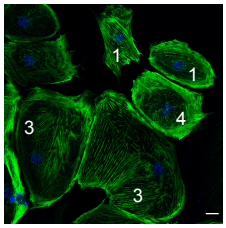

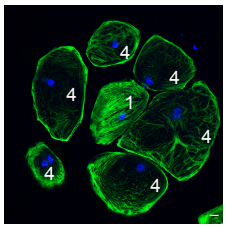

Score 4:
myofibrillar fragmentation or
aggregation > 50% cell volume

H

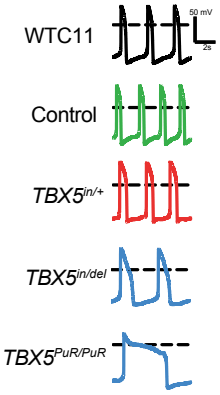

I

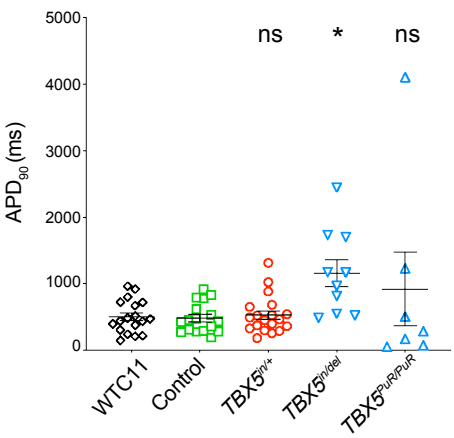

Figure S1. Genome editing of *TBX5* in human iPSCs, and additional phenotyping of iPSC-derived cardiomyocytes by *TBX5* genotype. Related to Figure 1. (A) Diagram of the human *TBX5* gene. Exons encoding the T-box domain of TBX5 are indicated in red. sgRNA1 was used to target exon 3 of *TBX5* by a CRISPR/Cas9 nuclease. (B) Sequence of the exon 3 of *TBX5* is shown, along with the sgRNA1 location. The PAM site is boxed in blue. Loss of the NlaIII site at the PAM site was used in initial screening for mutant iPS cell clones by PCR. The encoded wildtype protein sequence includes the start of the T-box domain. (C) Sequence and chromatogram for the 2bp insertion of the mutant allele for $TBX5^{in/+}$ predicts a premature truncation, as indicated by a stop codon (white asterisk in red box) in the frame-shifted protein sequence. (D, E) Sequence and chromatogram for the 1 bp insertion, or 8 bp deletion, respectively, of the mutant allele for $TBX5^{in/del}$, along with corresponding protein sequences, are shown. (F) Table shows genotypes of WTC11-derived iPS cell lines that were targeted for *TBX5* at exon 3. Predicted translation for each *TBX5* genotype is indicated. (G) Myofibrillar arrangement in cardiomyocytes was manually scored on a scale of 1-5, similar to (Judge et al., 2017). No cells displayed a score above 4. Sample sizes were as follows (WTC11 n=97, Control n=129, $TBX5^{in/+}$ n=53, $TBX5^{in/del}$ n=69). Scale bar: 25 microns. (H) Action potentials by patch clamp of single beating cells for each *TBX5* genotype. (I) Action potential duration at 90% (APD_{90}) (* FDR<0.05).

Figure S2

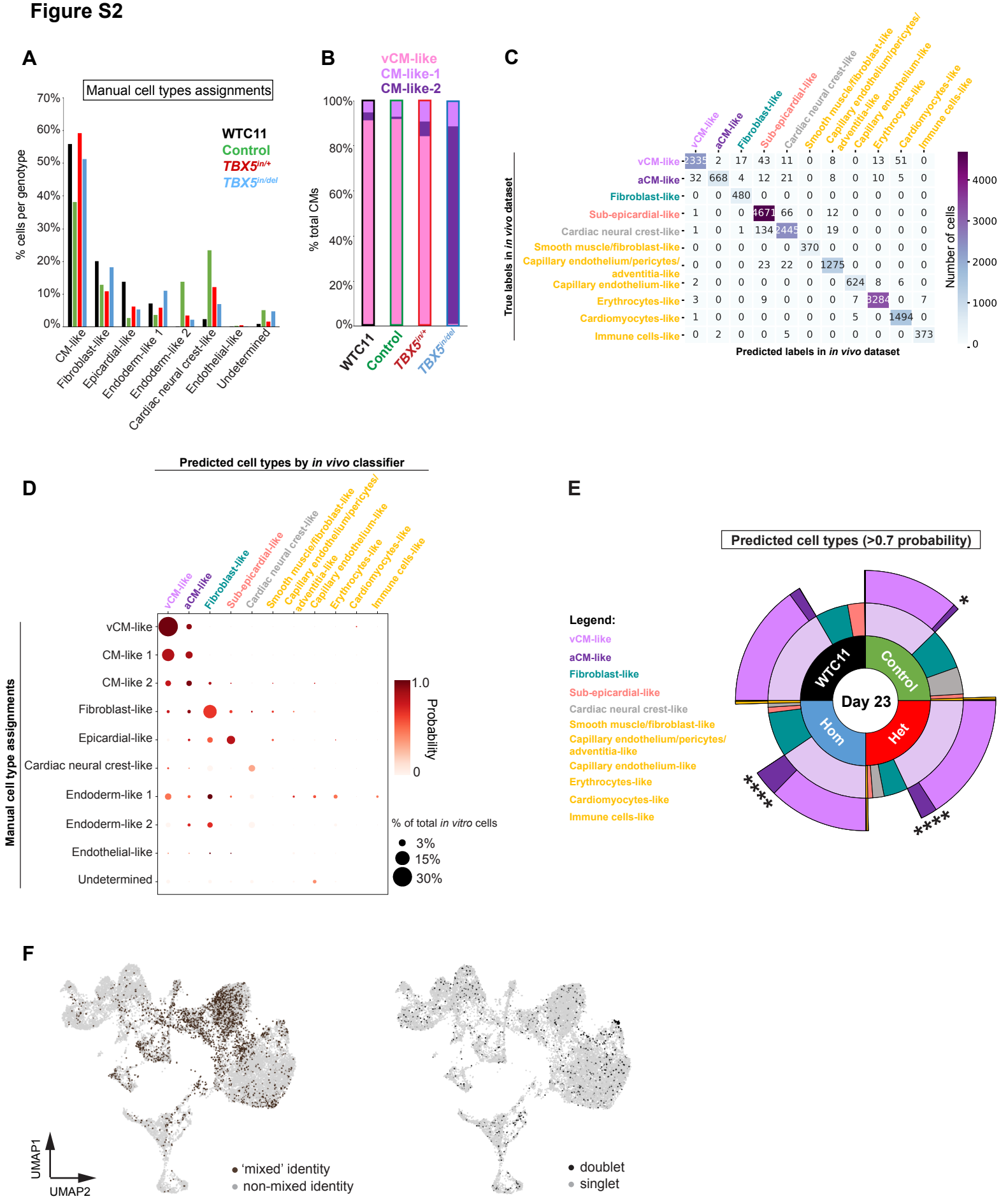
A
Manual cell types assignments
% cells per genotype
70%
60%
50%
40%
30%
20%
10%
0%
WTC11
Control
TBX5in/+
TBX5in/del
CM-like
Fibroblast-like
Epicardial-like
Endoderm-like 1
Endoderm-like 2
Cardiac neural crest-like
Endothelial-like
Undetermined
B
vCM-like
CM-like-1
CM-like-2
% total CMs
100%
80%
60%
40%
20%
0%
WTC11
Control
TBX5in/+
TBX5in/del
C
True labels in in vivo dataset
Predicted labels in in vivo dataset
vCM-like 2335 2 17 43 11 0 8 0 13 51 0
aCM-like 32 668 4 12 21 0 8 0 10 5 0
Fibroblast-like 0 0 480 0 0 0 0 0 0 0 0
Sub-epicardial-like 1 0 0 4671 66 0 12 0 0 0 0
Cardiac neural crest-like 1 0 1 134 2445 0 19 0 0 0 0
Smooth muscle/fibroblast-like 0 0 0 0 0 370 0 0 0 0 0
Capillary endothelium/pericytes/adventitia-like 0 0 0 23 22 0 1275 0 0 0 0
Capillary endothelium-like 2 0 0 0 0 0 0 624 8 6 0
Erythrocytes-like 3 0 0 9 0 0 0 7 3284 0 7
Cardiomyocytes-like 1 0 0 0 0 0 0 5 0 1494 0
Immune cells-like 0 2 0 0 5 0 0 0 0 0 373
Number of cells
4000
3000
2000
1000
0
D
Predicted cell types by in vivo classifier
Manual cell type assignments
vCM-like
CM-like 1
CM-like 2
Fibroblast-like
Epicardial-like
Cardiac neural crest-like
Endoderm-like 1
Endoderm-like 2
Endothelial-like
Undetermined
Probability
1.0
0
% of total in vitro cells
3%
15%
30%
E
Predicted cell types (>0.7 probability)
Legend:
vCM-like
aCM-like
Fibroblast-like
Sub-epicardial-like
Cardiac neural crest-like
Smooth muscle/fibroblast-like
Capillary endothelium/pericytes/adventitia-like
Capillary endothelium-like
Erythrocytes-like
Cardiomyocytes-like
Immune cells-like
WTC11
Control
Hom
Het
Day 23
*
****
****
F
UMAP1
UMAP2
'mixed' identity
non-mixed identity
doublet
singlet

Figure S2. Diversity of iPSC-derived cell types by *TBX5* genotype. Related to Figure 2. (A) Manual assignment of iPSC-derived cell types by *TBX5* genotypes at day 23. (B) Distribution of iPSC-derived cardiomyocyte classification by *TBX5* genotype at day 23. (C) A confusion matrix compares test vs. predicted cell type labels for human fetal cardiac cells (Asp et al., 2019). (D) A confusion matrix compares cell type assignments of iPSC-derived cells at day 23 by manual annotation and *in vivo* classifier prediction. Color of each dot represents a prediction probability of the *in vivo* cell type classifier, while the dot size displays the percentage of the total iPSC-derived cells at day 23. (E) Distribution for predicted cell types of >0.7 prediction probability is shown by *TBX5* genotype at day 23 in a sunburst plot. * $p<0.02$, **** $p<0.0001$ by Fisher's exact test. (F) UMAPs display predicted 'mixed' cells and estimated doublets.

Figure S3

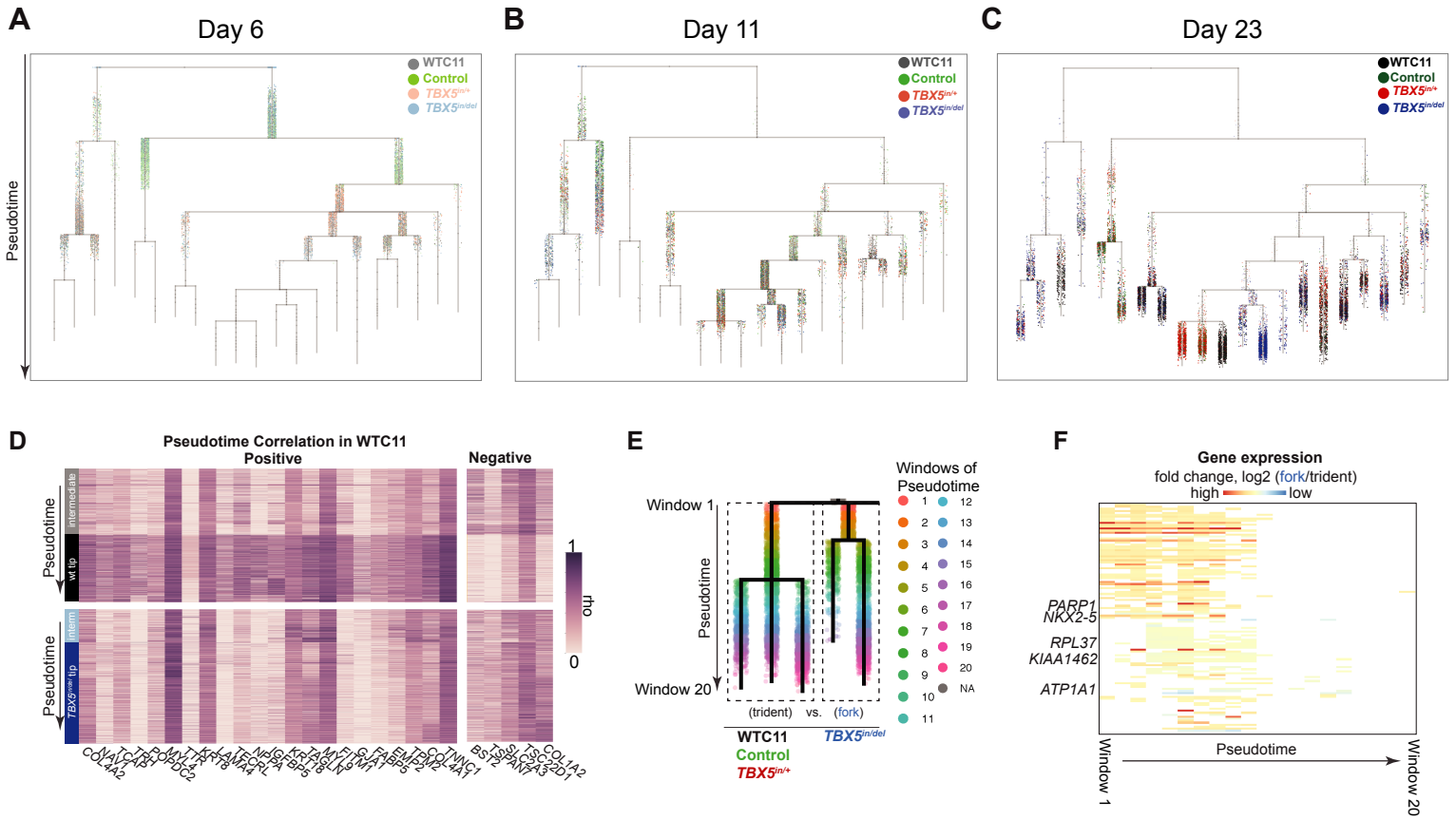

Figure S3. Pseudotime analysis of TBX5-dependent cardiomyocyte differentiation. Related to Figure 3. (A-C) Cells from all *TBX5* genotypes at day 6, 11 or 23 are shown by harvested time point on an aggregate pseudotime dendrogram using URD trajectory inferences. (D) Heatmaps show expression for each gene that displays a positive or negative correlation with pseudotime (|rho|≥0.4 and Z-score≥15 by difference in rho) in the WT path (above) and is altered in the *TBX5*$^{in/del}$ path (below). (E) Paths for WT/*TBX5*$^{in/+}$(trident) or *TBX5*$^{in/del}$ (fork) to cardiomyocytes were divided into windows (1-20) along pseudotime for comparison. (F) Heatmap shows fold change for genes in a cluster that includes *NKX2-5*, which was significantly different after correction (adj p<0.05 by Bonferroni-Holm test) in windows 2 through 8 between the deduced WT/control/*TBX5*$^{in/+}$ and *TBX5*$^{in/del}$ paths, along with genes of a similar pattern, including *PARP1*, *RPL37*, *KIAA1462*, and *ATP1A1* (adj p<0.05 by Bonferroni-Holm test).

Figure S4

A

	Stepwise response (85)	Downregulated genes (413) *TBX5*$^{in/+}$	Downregulated genes (313) *TBX5*$^{in/del}$	Upregulated genes (401) *TBX5*$^{in/+}$	Upregulated genes (289) *TBX5*$^{in/del}$
Genes near TBX5 binding sites (5762)	**72%** (61)	**64%** (263)	**58%** (183)	**56%** (223)	**55%** (158)
Genes near GATA4 binding sites (3207)	**49%** (42)	**42%** (174)	**37%** (117)	**41%** (163)	**40%** (116)
Genes near TBX5+GATA4 binding sites (2185)	**47%** (40)	**37%** (154)	**34%** (107)	**34%** (136)	**34%** (97)

high — low: percent overlap

B

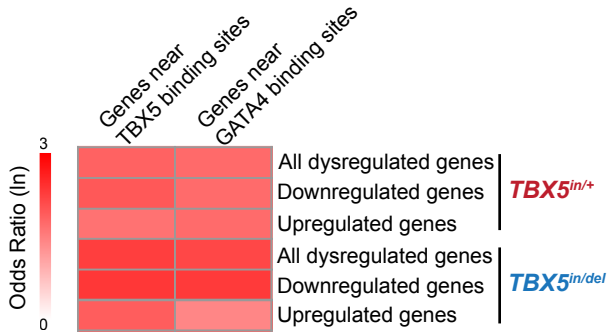

C

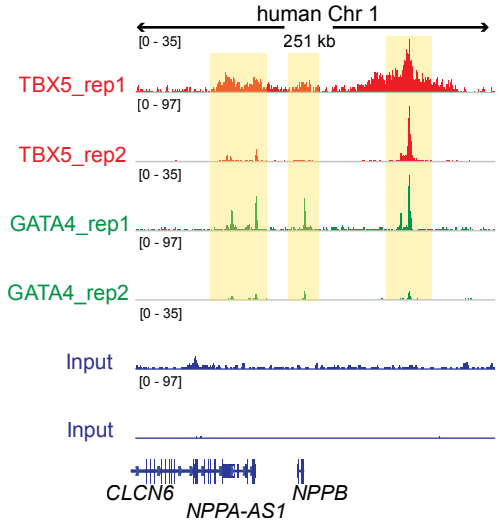

D

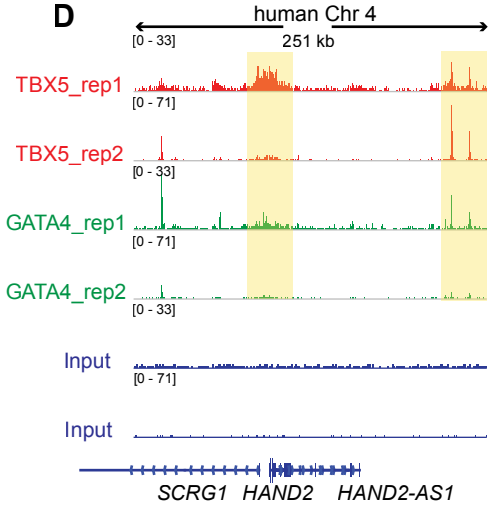

E

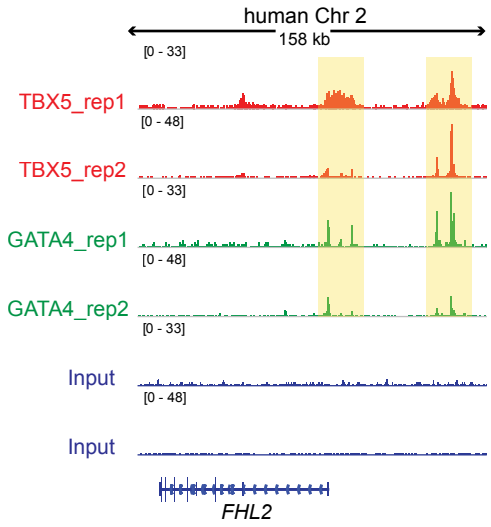

F

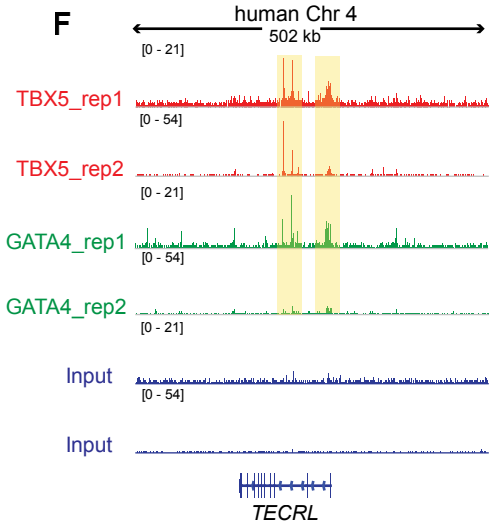

Figure S4. TBX5 and GATA4 occupancy near human TBX5-dependent genes. Related to Figure 4. (A) Table shows number of TBX5-dependent genes near TBX5, GATA4 or TBX5 and GATA4 occupancy (Ang et al., 2016). (B) Heatmap displays significant correlations (FDR<0.05) of TBX5 or GATA4 occupancy near human TBX5-dependent gene sets (Table S5). Odds ratios for co-occupancy of TBX5 and GATA4 at TBX5-dependent genes are in Table S5. (B-E) Browser tracks of TBX5 and GATA4 occupancy from iPSC-derived cardiomyocytes are shown for loci of TBX5-dependent genes *NPPA/NPPB*, *HAND2, FHL2* and *TECRL.*

Figure S5

A

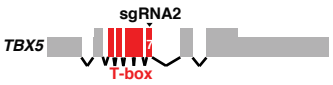

B

	Genotype	Translation
Parental (PGP1)	+/+	
+Cas9 *TBX5*$^{+/in}$	+/ins 1bp	+/p.G235fs*2
+Cas9 *TBX5*$^{del/del}$	del 7bp/del 7bp	p.G235fs*26/p.G235fs*26

C

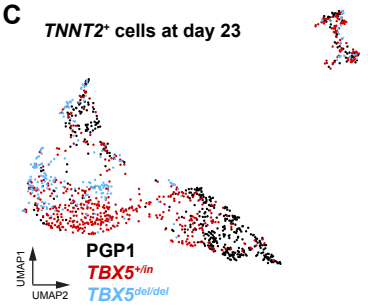

D

H

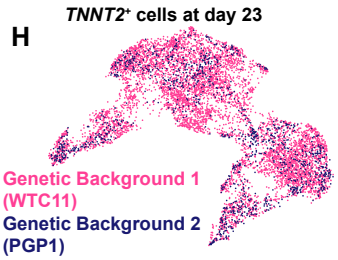

I

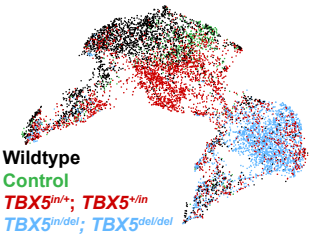

J

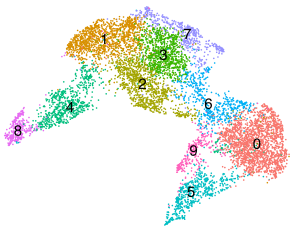

K

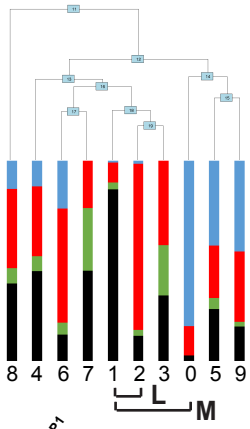

E

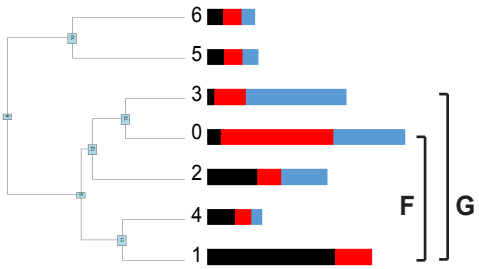

F

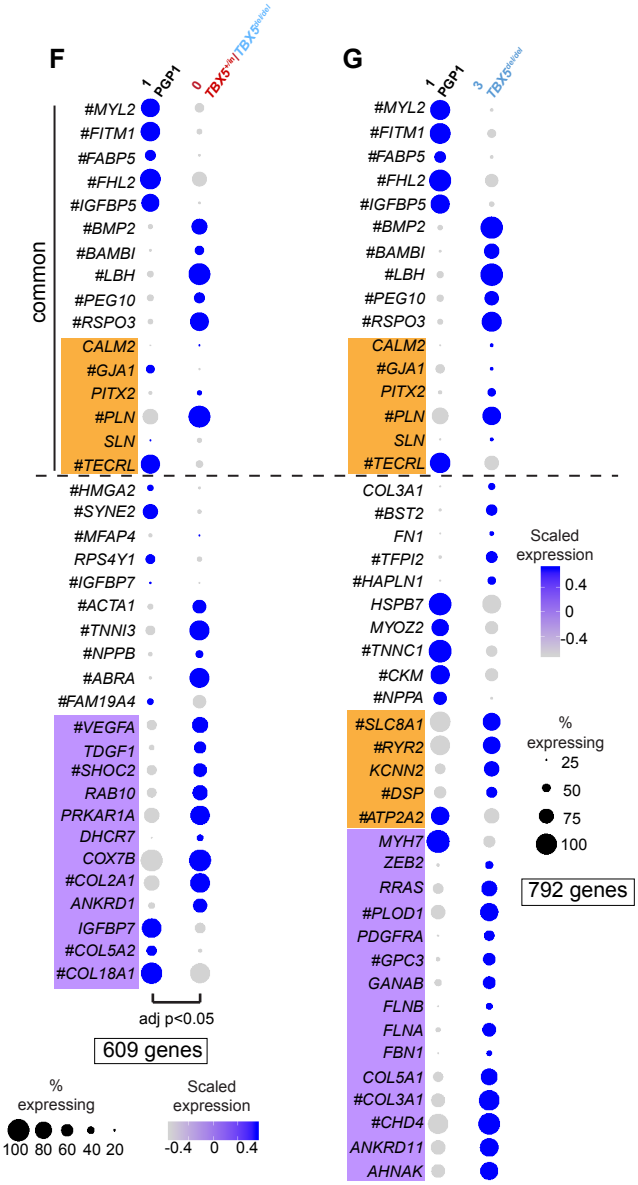

G

L

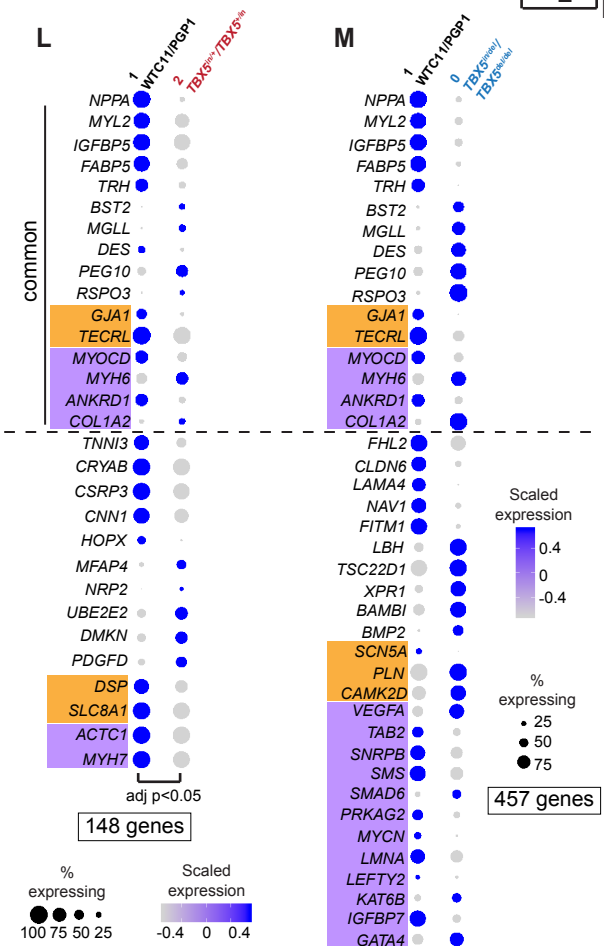

M

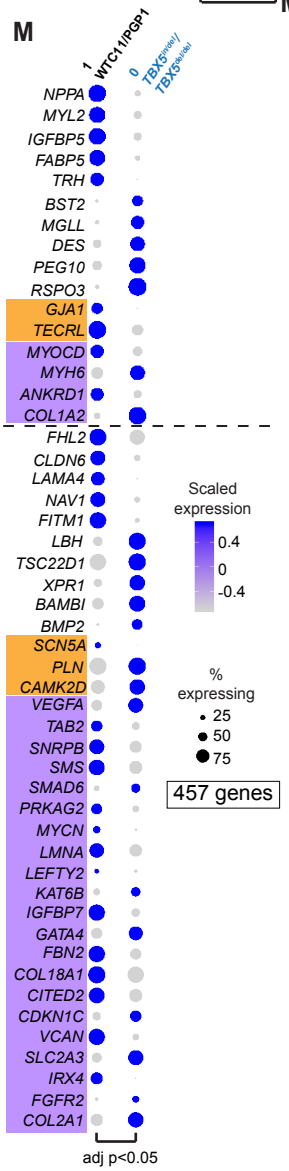

Figure S5. Assessment of two genetic backgrounds for TBX5 dose-sensitive gene expression. Related to Figure 4. (A) Diagram of the human *TBX5* gene is shown, with exons in red. The guide sgRNA2 was used to target exon 7, which encodes a portion of the T-box domain, of *TBX5* in PGP1 iPS cells. (B) A table specifies each *TBX5* mutation and the predicted translation of TBX5 for PGP1-derived $TBX5^{+/in}$ or $TBX5^{del/del}$ cells. (C, D) UMAPs of $TNNT2^{+}$ cells at day 23 by *TBX5* genotype (C) or cluster identity (D). (E) A phylogenetic tree shows the relatedness of the 'average' cell in each cluster using PC space. The percentage of cells within a cluster from each *TBX5* genotype are colored. Related clusters between different *TBX5* genotypes were compared for differential gene expression. (F, G) Dot plots show top differentially expressed genes in (F) $TBX5^{+/in}$- or (G) $TBX5^{del/del}$-enriched clusters. Significance was determined by Wilcoxon Rank Sum test (adj $p<0.05$) (Table S2). #: Genes commonly dysregulated between two genetic backgrounds. (H-J) $TNNT2^{+}$ cells are displayed in a UMAP, by genetic background (WTC11 or PGP1-derived cells) (H), by *TBX5* genotype (I), or by Louvain clustering (J). We define *TBX5* Het to reflect both cell lines ($TBX5^{in/+}$ derived from WTC11, $TBX5^{+/in}$ derived from PGP1) and *TBX5* Hom to reflect both cell lines ($TBX5^{in/del}$ from WTC11, $TBX5^{del/del}$ from PGP1). (K) A phylogenetic tree shows the relatedness of the 'average' cell in each cluster using PC space. The proportion of cells in each cluster are colored by *TBX5* genotype. Related clusters between different *TBX5* genotypes were selected for differential gene tests. (L, M) Dot plots show top differentially expressed genes in (L) $TBX5^{+/in}$- or (M) $TBX5^{del/del}$-enriched clusters. Top five upregulated or downregulated differentially expressed genes, along with EP and CHD genes, were common between comparisons. Significance was determined by Wilcoxon Rank Sum test (adj $p<0.05$) (Table S2, S3).

Figure S6

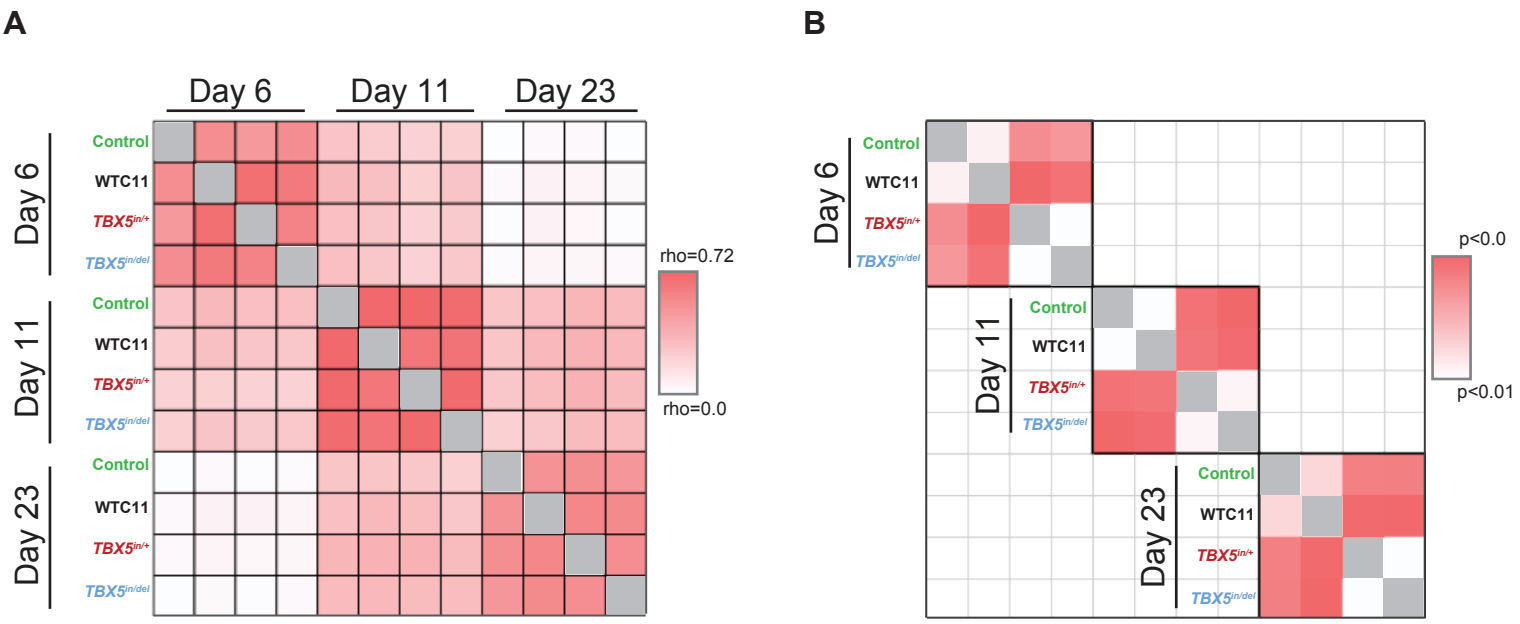

Figure S6. Analysis of TBX5 dosage-sensitive gene regulatory networks. Related to Figure 6. (A) Correlation plot (Pearson correlations of pagerank centralities) of *TNNT2*$^{+}$ networks by *TBX5* genotypes and time points are shown. Note that networks display highest similarity (red) within a time point. An inter-stage dissimilarity (white) grows proportionally to the time difference (i.e. day 23 is less similar to day 6 than to day 11). Therefore, comparisons for genotype differences were made within differentiation stages. (B) Network similarity among *TBX5* genotypes within each time point is shown (Wilcoxon Rank Sum test of pagerank centralities for nodes from selected time point comparisons).